PCCP

ROYAL SOCIETY OF CHEMISTRY

PAPER

View Article Online
View Journal | View Issue



Cite this: *Phys. Chem. Chem. Phys.*, 2022, **24**, 3017

# Selective decomposition of hydrazine over metal free carbonaceous materials†

Ilaria Barlocco,[a] Silvio Bellomi,[a] Simone Tumiati,[b] Patrizia Fumagalli,[b] Nikolaos Dimitratos,[c] Alberto Roldan *[d] and Alberto Villa *[a]

Herein we report a combined experimental and computational investigation unravelling the hydrazine hydrate decomposition reaction on metal-free catalysts. The study focuses on commercial graphite and two different carbon nanofibers, pyrolytically stripped (CNF-PS) and high heat-treated (CNF-HHT), respectively, treated at 700 and 3000 °C to increase their intrinsic defects. Raman spectroscopy demonstrated a correlation between the initial catalytic activity and the intrinsic defectiveness of carbonaceous materials. CNF-PS with higher defectivity ($I_D/I_G$ = 1.54) was found to be the best performing metal-free catalyst, showing a hydrazine conversion of 94% after 6 hours of reaction and a selectivity to $H_2$ of 89%. In addition, to unveil the role of NaOH, CNF-PS was also tested in the absence of alkaline solution, showing a decrease in the reaction rate and selectivity to $H_2$. Density functional theory (DFT) demonstrated that the single vacancies (SV) present on the graphitic layer are the only active sites promoting hydrazine decomposition, whereas other defects such as double vacancy (DV) and Stone–Wales (SW) defects are unable to adsorb hydrazine fragments. Two symmetrical and one asymmetrical dehydrogenation pathways were found, in addition to an incomplete decomposition pathway forming $N_2$ and $NH_3$. On the most stable hydrogen production pathway, the effect of the alkaline medium was elucidated through calculations concerning the diffusion and recombination of atomic hydrogen. Indeed, the presence of NaOH helps the extraction of H species without additional energetic barriers, as opposed to the calculations performed in a polarizable continuum medium. Considering the initial hydrazine dissociative adsorption, the first step of the dehydrogenation pathway is more favourable than the scission of the N–N bond, which leads to $NH_3$ as the product. This first reaction step is crucial to define the reaction mechanisms and the computational results are in agreement with the experimental ones. Moreover, comparing two different hydrogen production pathways (with and without diffusion and recombination), we confirmed that the presence of sodium hydroxide in the experimental reaction environment can modify the energy gap between the two pathways, leading to an increased reaction rate and selectivity to $H_2$.

Received 12th November 2021,
Accepted 24th December 2021

DOI: 10.1039/d1cp05179b

rsc.li/pccp



## Introduction

Green and sustainable sources of energy are essential to mitigate the environmental impact of fossil fuels and the rising energy demand. Hydrogen has been recognised as one of the most suitable alternative energy vectors due to its high energy and innocuous products upon utilisation.[1] Despite its benefits, the direct usage of hydrogen is inhibited by the scarcity of economical and safe hydrogen storage technologies.[2] Hence, alternative approaches to store and transport hydrogen,[3–6] and materials that release it under mild conditions, are urgently required.[7]

Hydrazine ($N_2H_4$) can be employed as a hydrogen carrier because it is liquid at $T < 114$ °C (1 atm) and can be easily transported.[8–11] In addition, it is a carbon-free fuel, and hence avoids undesired emissions, *e.g.* $CO_2$, and species damaging the catalysts as seen in the CO poisoning of Pt/C electrodes in proton exchange membrane fuel cells (PEMFCs).[12,13] Currently, the $N_2H_4$ exothermic decomposition is employed as a propellant in aerospace applications, *i.e.*, in rockets and artificial satellites.[14,15] $N_2H_4$ possesses a hydrogen content of 12.5 wt%[16] and decomposes into a mixture of ammonia, hydrogen and

[a] *Dipartimento di Chimica, Università degli Studi di Milano, via Golgi 19 Milano I-20133, Italy. E-mail: alberto.villa@unimi.it*
[b] *Dipartimento di Scienze della Terra Ardito Desio, Università degli Studi di Milano, via Mangiagalli 34, Milano I-20133, Italy*
[c] *Dipartimento di Chimica Industriale e dei Materiali, ALMA MATER STUDIORUM Università di Bologna, Viale Risorgimento 4, Bologna 40136, Italy*
[d] *Cardiff Catalysis Institute, School of Chemistry, Cardiff University, Main Building, Park Place, CF10 3AT, Cardiff, UK. E-mail: RoldanMartinezA@cardiff.ac.uk*

† Electronic supplementary information (ESI) available. See DOI: 10.1039/d1cp05179b

nitrogen in the presence of catalysts such as Shell 405 (30 wt% $Ir/Al_2O_3$).[17,18] $N_2H_4$ decomposition occurs in two different pathways:[19–21]

$$N_2H_4 \rightarrow N_2\,(g) + 2H_2\,(g) \quad \Delta H^\circ = -95.4\ \text{kJ mol}^{-1} \qquad (1)$$

$$3N_2H_4 \rightarrow N_2\,(g) + 4NH_3\,(g) \quad \Delta H^\circ = -157.0\ \text{kJ mol}^{-1} \qquad (2)$$

The first reaction (eqn (1)) represents the complete reforming pathway, where molecular hydrogen and nitrogen are produced. The second reaction (eqn (2)) is thermodynamically favoured and produces ammonia and nitrogen. The selectivity of the reaction can vary with the variation of experimental reaction conditions, such as pressure, temperature and the choice of catalyst present.[22–25] In a typical hydrazine catalytic decomposition process on metal surfaces, the molecule adsorbs on the catalyst surface (below marked with an asterisk) driving the N–N or the N–H cleavage. From a thermodynamic point of view, the cleavage of the N–N bond (eqn (3)) is favored compared to the N–H bond dissociation energy (BDE, eqn (4)).[26,27] Hence, the nature of the catalyst plays a crucial role in quenching the incomplete decomposition pathway (eqn (2)) and promoting the cleavage of the N–H bond (eqn (4)).

$$N_2H_4^* \rightarrow H_2N^* + H_2N^* \quad \text{BDE} = 286.0\ \text{kJ mol}^{-1} \qquad (3)$$

$$N_2H_4^* \rightarrow H_3N_2^* + H^* \quad \text{BDE} = 360.0\ \text{kJ mol}^{-1} \qquad (4)$$

Because of its hypergolic nature, the risk of explosion is one of the most serious problems related to handling hydrazine, especially in the presence of a metal that may catalyse its decomposition.[28] One solution can be the dilution of $N_2H_4$ in an inert gas such as argon[25] or in water, forming hydrous hydrazine ($N_2H_4{\cdot}H_2O$), which can be particularly important as a liquid hydrogen source.[29] Hydrous hydrazine still contains 7.9 wt% of hydrogen, avoiding all the issues related to $H_2$ storage and transportation.[7,30] The development of a catalyst capable of exothermically reacting with $N_2H_4{\cdot}H_2O$ and selectively decomposing it into hydrogen is key for a $H_2$-based economy.[26,31] In order to generate hydrogen in a controlled manner and on-demand, different supported[32–34] and unsupported metal nanoparticles (NPs) have been investigated.[13,15,28] First of all, noble metals such as Ir[29,35] and Rh[10,36] performed well as reforming catalysts. Nevertheless, due to its cost and synergetic catalytic properties, Ni was introduced as the second metal providing superior activity and selectivity.[33,37–43]

The presence of NaOH in the hydrazine decomposition environment can favor its selective decomposition, suppressing the formation of $NH_3$. In particular, Wang *et al.* have demonstrated that adding a 0.5 M solution of NaOH to unsupported Ni NPs can enhance the selectivity to $H_2$ from 64% to 100%.[44] In addition, Peng and co-workers have performed theoretical and experimental studies on Pt-Ni/C catalysts showing a strong dependence of the selectivity and reaction rate with the pH.[45] Indeed, the presence of $OH^-$ facilitates the N–H scission and promotes $H_2$ and $H_2O$ formation.[11,46]

Despite the excellent activity, selectivity and relative stability of metal-based catalysts,[27,47–51] employing metals is raising reservations about the overall sustainability of hydrogen production reactions.[52–54] On the other hand, in the last few decades, carbon-based catalysts have been attracting significant attention for replacing metal-based materials in heterogeneous catalysis and making the production of chemicals and commodities greener and thus more sustainable. Different studies have demonstrated that metal-free carbon materials can be effective in gas phase reactions, in particular in the dehydrogenation of alkenes and alkanes,[55–57] and in liquid phase reactions, *i.e.*, oxidation of benzene[58] and alcohols,[59,60] and in reduction reactions such as acetylene, carbon–carbon multiple bonds and functionalized benzenes.[61,62]

Combining experimental and DFT studies, we reported recently the promising activity and selectivity of metal-free carbon catalysts in the generation of $H_2$ from formic acid.[63] In particular, we demonstrated that defects, especially single vacancies, are active in the formic acid dehydrogenation reaction even in the presence of oxygen groups. Similar investigations including a wide range of carbon dopants proved the same results in ammonia reforming.[64] Therefore, we decided to extend these findings to the hydrogen generation from hydrazine. To the best of our knowledge, the decomposition of hydrazine on a metal-free carbon-based catalyst has been reported only on g-$Si_3C$, which is able to adsorb $N_2H_4$ in its *anti*-configuration and decompose it following pathways different to those on metal surfaces.[65]

In the present work, different carbonaceous materials, *i.e.*, graphite and two different types of carbon nanofibers differing in the graphitization degree (PR24-PS and PR24-HHT), were employed in the liquid phase hydrazine decomposition reaction. A systematic density functional theory (DFT) study on $N_2H_4$ adsorption and decomposition was employed to understand the role of the defects in this process, paving the pathway to the development of new and efficient carbo-catalysts.

## Experimental method

### Materials and chemicals

CNFs PR24-PS and PR24-HHT were purchased from the Applied Science Company. These nanofibers were prepared at different post-treatment temperatures, in order to remove polyaromatic carbon layers covering their external surface. The thermal treatments were performed at 700 and 3000 °C for PR24-PS and PR24-HHT, respectively in order to study different graphitization degrees. Graphite was obtained from Johnson Matthey. $N_2H_4{\cdot}H_2O$ (98%), sodium hydroxide (NaOH, ≥98%), hydrochloric acid (HCl, 37% wt) and 4-dimethylaminobenzaldehyde (4-DMAB, 98%) were acquired from Sigma-Aldrich.

### Catalytic tests

Liquid phase $N_2H_4{\cdot}H_2O$ decomposition was performed at a constant reaction temperature of 50 °C using a 50 mL three-necked round bottom flask, with one of the flask's neck connected with a burette employed for gas volume analyses.

Typically, the required amount of catalyst (hydrous hydrazine/catalyst weight ratio 15.7/1) was added in the reactor, where

 

16.0 mL of a 0.5 M NaOH aqueous solution was placed and heated at the desired temperature. Once the solution reached the desired temperature, 600 μL of a 3.3 M hydrous hydrazine aqueous solution was inserted and the final mixture was stirred at 1400 rpm using a magnetic stirrer.

### Product analyses

Hydrous hydrazine conversion was analysed using a Jasco V-730 spectrophotometer, using a 1 cm quartz cell. The conversion was calculated according to the equation $mol_{in} - mol_{out}/(mol_{in} \times 100)$, where $mol_{in}$ and $mol_{out}$ are the initial and the remaining moles, respectively. The analytical method was based on the reaction of $N_2H_4{\cdot}H_2O$ with 4-dimethylaminobenzaldehyde (4-DMAB) in dilute hydrochloric acid (Scheme 1). The substrate quantitatively reacts with 4-DMAB to give a *p*-quinone structure that adsorbs at 456 nm.[66,67] The concentration was calculated using the Beer–Lambert equation.

The volume of gas produced was measured using the water displacement method. The gaseous products released were allowed to pass to a trap containing a 0.05 M HCl aqueous solution to ensure the removal of $NH_3$, if any, and volumetrically monitored employing the burette. Using this method, the volume measured was only due to $N_2$ and $H_2$ molecules, enabling us to evaluate $n(N_2 + H_2)$. The selectivity to hydrogen ($x$) was then calculated according to eqn (5):[44]

$$3NH_2NH_2 \rightarrow (1 + 2x)N_2 + 6xH_2 + 4(1 - x)NH_3 \quad (5)$$

Considering the molar ratio $n(N_2 + H_2)/n(N_2H_4)$ ($\lambda$), $x$ can be evaluated as eqn (6):

$$x = \frac{3\lambda - 1}{8} \quad (6)$$

### Catalyst characterization

Carbon samples were characterized by ICP-OES and Raman spectroscopy. Raman spectroscopy was executed using a Horiba LabRam HR Evolution micro-Raman spectrometer equipped with a green solid-state laser (532 nm) focused through a 100× objective, giving a spatial resolution of approximately 1 μm. The micro-Raman system was set with 300 lines per mm grating and a hole of size 300 μm; the spectrum was collected with a final laser power of about 0.05 mW. The sample surface was measured through a hand-held power meter. Spectra were calibrated using the 520.7 $cm^{-1}$ line of a silicon wafer. The sample was scanned at an exposure time of 300 s and 2 accumulations were performed giving a spectrum. The presence of possible residual metal was analysed by inductively coupled plasma optical emission spectroscopy (ICP-OES) using a PerkinElmer Optima 8000 emission spectrometer.

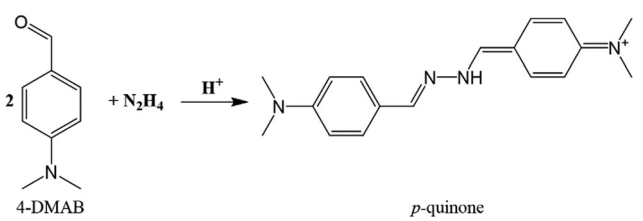


Scheme 1 Reaction of 4-DMAB and hydrazine to give the yellow *p*-quinone.

### Computational method

Periodic plane-wave density functional theory (DFT) calculations were carried out using the Vienna Ab initio Simulation Package (VASP).[68,69] The generalized gradient approximation from the revised Perdew–Burke–Ernzerhof approximation (RPBE)[70] has been used to take into account the correlation-exchange electronic contributions, with a kinetic energy cutoff of 500 eV chosen for the expansion of the Kohn–Sham valence state plane-waves.[71] RPBE is an improved version of the revPBE implementation,[72] fulfilling the Lieb-Oxford criterion globally by construction and without the need for further parameter fitting. Similarly to other XC potentials, care must be taken when discussing simulation results, *e.g.* metal overstabilization effects.[70] All the calculations include the long-range dispersion correction approach by Grimme–DFT-D3 methods,[73,74] an improvement on pure DFT to evaluate molecular interactions.[75–78] We also included the implicit solvation model as implemented in VASPsol,[79,80] where the solvent is considered as a polarizable continuum dielectric bath. The optimization thresholds for electronic and ionic force relaxation were, respectively, $10^{-5}$ eV and 0.02 eV $Å^{-1}$. For Brillouin zone sampling, a $\Gamma$-centered *k*-point mesh was generated through the Monkhorst–Pack method of dimensions 5 × 5 × 1 in order to avoid Pulay stress.[81] To improve the convergence of the Brillouin-zone, a first order Methfessel–Paxton method has been used with an energetic width value of 0.2 eV. All carbon-based materials were modelled starting from a single layer slab of a 6 × 6 pristine graphene supercell and introduced different defects: single vacancy (SV), double vacancy (DV) and three different Stone Wales defects (SW1, SW2, and SW3).[63] The supercell is in a hexagonal crystalline system with unit cell vectors *a* and *b* lying in the surface plane and perpendicular to the *c* axis. Both, *a* and *b*, were optimized at 14.8 Å, in good agreement with experimental values obtained by Transmission Electron Aberration-corrected Microscopy (TEAM).[82] We introduced a polarizable continuum dielectric bath of ∼16 Å perpendicular to the C-surface in order to avoid spurious periodic interactions with periodic images. Computational characterization of the surfaces was performed using the Bader analysis as implemented by Henkelmann *et al.*[83] A fast convergence of charges with respect to the Fast Fourier Transform grid was obtained employing the Grid Method by Yu,[84] which quadratically converges charge values with respect to mesh size. A grid of 370 × 370 × 390 points was applied in order to optimize memory usage and precision of the calculations. These values were obtained converging two equivalent carbon charges in pristine graphene. Charge density local curvatures, local accumulations and depletions were evaluated to disclose the ability of every inequivalent surface site to adsorb and decompose hydrazine. The optimized parameters obtained from the grid method were employed in a Laplacian topological analysis.[85] The AIM-UC Bader Analysis Toolkit implemented by David Vega *et al.*[86] was applied on the total

electron density obtained combining the valence charge data and the core charges, resulting in the Laplacian of the charge density map, which allowed analysis of Bond Critical Points (BCPs). Before adsorbing the hydrazine molecule, a systematic study on all possible active sites was performed using $NH_3$ as a probe molecule considering both dissociative and non-dissociative adsorption modes. The molecular adsorption energy ($E_{ADS}$) was defined as the difference between the energies of the combined system and the isolated species. The reaction energy ($E_R$) of each $N_2H_4$ dissociation elementary step was described as the total energy difference between those of the final (final adsorbate/C) and the initial states (initial adsorbate/C). Hydrogen diffusion calculations were performed on the single vacancy (SV) system, which proved to be the most active defect in this study. A hydrogen atom was placed in the desired position where only its $z$ coordinate could relax during the optimization calculations. Later on, all carbon atoms were allowed to relax except two of them that were sufficiently far from the active site to avoid rotations or translations of the considered surface as a whole.[87] The hydrogen diffusion energy ($E_D$) was calculated as the energy difference between atomic hydrogen within the vacancy, in the most stable configuration, and the diffused atomic hydrogen structures.

## Results

Different carbonaceous materials with different graphitization degrees (CNF-PS, CNF-HHT and graphite) were employed as catalysts for the hydrous hydrazine reforming reaction, to elucidate the possible role of the carbon defects in the catalytic performance. Moreover, the effect of the presence of a base was evaluated by testing the materials with or without NaOH.

### Characterization and catalytic activity

ICP-OES analysis confirmed the absence of possible metallic impurities. The reaction conditions were optimized to assess the reaction kinetic regime and to establish the correct amount of catalyst to be used. The optimum conditions were 50 °C and 1400 rpm, using 600 μL of a hydrazine solution 3.3 M in 16 mL of NaOH 0.5 M and a $N_2H_4{\cdot}H_2O$:catalyst weight ratio of 15.7 : 1. To ensure reproducibility, all the experiments were repeated three times. Fig. 1 shows the different kinetic profiles for 6 h of reaction. CNF-PS exhibited the highest conversion at 6 h (94%), whereas CNF-HHT and graphite showed similar conversion (71% and 65%, respectively) (Table 1, column 4).

On the most active material, CNF-PS, $H_2$ selectivity was calculated using the water displacement method and 89% selectivity for the complete hydrazine decomposition reaction was determined. In order to rationalize these results in terms of structural properties, we characterized all the catalysts using Raman spectroscopy. It allowed us to investigate the graphitization degree of carbon materials measuring the two bands at around 1600 $cm^{-1}$ (G band) and 1350 $cm^{-1}$ (D band).[88] The G band is generated by the C=C stretching vibrations in the graphite lattice, and it is related to structurally ordered graphite domains. The D band corresponds to the $A_{1g}$ mode, which is forbidden according to the selection rules in graphite, but is active in the presence of structural defects or in-plane substitutional heteroatoms.[88] All carbon materials studied in this work present both D and G Raman bands with the following $I_D/I_G$ ratio: CNF-PS (1.54) > graphite (0.20) > CNF-HHT (0.11) (Table 1).

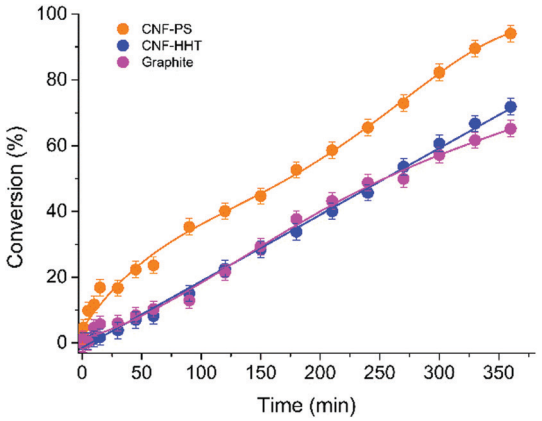


Fig. 1 Conversion trend for the hydrazine decomposition reaction for the different carbonaceous materials: graphite (violet), CNFs PR24-PS (orange) and PR24-HHT (blue). All the tests were performed at 50 °C and 1400 rpm, using 600 μL of a 3.3 M hydrazine solution in 16 mL of 0.5 M NaOH and a $N_2H_4{\cdot}H_2O$:catalyst weight ratio of 15.7 : 1.

Table 1 Raman characteristics of the carbon catalyst, their initial catalytic activity (15 minutes of reaction) and final conversion towards hydrazine decomposition (6 h)

| | Raman $I_D/I_G$ | Activity at 15 min ($mg^{-1}$ $min^{-1}$) × $10^2$ | Conversion at 6 h (%) |
|---|---|---|---|
| Graphite | 0.20 | 6.0 | 65 |
| CNF-PS | 1.54 | 18 | 94 |
| CNF-HHT | 0.11 | 1.9 | 71 |

To unveil the effect of NaOH in the reaction environment, the most active material (*i.e.* CNF-PS) was tested under the same experimental conditions, in the absence of NaOH, but with distilled water as the solvent. From the comparison between the reaction profiles shown in Fig. 2, it is clear that the presence of NaOH affects not only the selectivity of the reaction, but also its kinetics.[11,46] Indeed, the catalyst tested under the same conditions with NaOH exhibited about 70% hydrous hydrazine conversion for 4 h of reaction, while the same material tested in water presented a 15% conversion.

### DFT study

Systematic DFT simulations were performed to elucidate the roles of carbon defects in hydrazine activation and decomposition and explain the presented experimental results. Six different graphitic surfaces were modelled: pristine graphite (PG), single vacancy (SV), double vacancy (DV) and three different Stone–Wales defects (SW, VSW1, and VSW2), represented in Fig. S1 (ESI†).

### Hydrazine adsorption

Prior to proceeding with the adsorptions, we performed an evaluation of charge density at Bond Critical Points (BCPs)[89] to

 

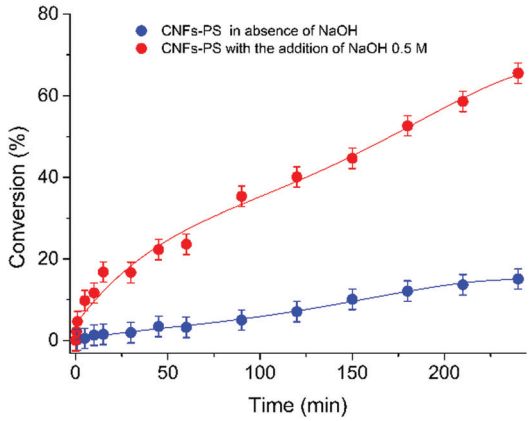


Fig. 2 Comparison of conversion trend for hydrazine decomposition in a different reaction environment. Alkaline aqueous solvent, red solid line, and distilled water, blue solid line. All the tests were performed at 50 °C and 1400 rpm, using 600 μL of a 3.3 M hydrazine solution in 16 mL of solvent (0.5 M NaOH for the red profile, distilled water for the blue one) and a $N_2H_4{\cdot}H_2O$ : catalyst weight ratio of 15.7 : 1.

estimate the potential active sites of the different optimized surfaces (Fig. S2, ESI†). As previously shown, only sites presenting distortions in the graphene π-system are able to interact favourably with adsorbates.[64] The obtained electron densities measured on the defects are summarised in Table 2. It was observed that only SV and DV are potential catalyst candidates to bind $N_2H_4$ as these two structures contain dangling C-atoms lacking electron density.[63] This result underlaid the localization of the catalytic site on both SV and DV. We validated the assumptions regarding the active sites by using ammonia ($NH_3$) as a probe molecule (Tables S1 and S2, ESI†). It was brought near non-equivalent active sites and the system relaxed. In line with previous studies, the graphitic areas possess an inactive π-conjugation, not sensitive to adsorption of molecules.[64,90–92] Only single vacancies showed a favourable (exothermic) interaction with ammonia, indicating that a $\rho(\vec{r}_{BCP})$ smaller than 0.6 $e^-$ $A^{-3}$ defines the active sites on carbon surfaces. Combining the Laplacian of charge density analysis and the performed tests with $NH_3$, we were able to identify $C_3$, $C_{3'}$ and $C_7$ in the single vacancy system as possible active sites (Fig. 3). Then, hydrazine was placed and relaxed on such sites with different initial orientations. We also investigated the molecule dissociative adsorption,[93,94] *i.e.*, breaking the N–H or N–N bonds while forming a new one with the surface similar to those in previous works on metal surfaces.

Table 2 Charge density at the bond critical points of the potential active sites

| Surface Site | $\rho(\vec{r}_{BCP})$/$e^-$ $Å^{-3}$ |
|---|---|
| PG | 2.03 |
| SV | 0.587 |
| DV | 0.974 and 0.979 |
| SW | 1.863–2.589 |
| VSW1 | 1.628–2.156 |
| VSW2 | 1.602–2.134 |

The least stable $N_2H_4$ adsorption configuration is the anti-single linked (a-SL) configuration where hydrazine interacted with only one carbon atom ($C_3$) (Fig. 4a). When the molecule is bonded to two active sites in a bridge configuration, it may adopt the *cis*-bridged (*c*B–H) configuration driving the N–H dissociation (Fig. 4b) or the *cis*-bridged (*c*B–N) structure resulting in the N–N bond scission (Fig. 4c). It can be seen from the adsorption energies inserted in Fig. 4 that the resulting stability increases following the sequence a-SL < *c*B-N < *c*B-H. Zheng *et al.* investigated the same adsorption process on metal-free $SiC_3$ siligraphene resulting in the following stability sequence: *cis*-$N_2H_4$ < *gauche*-$N_2H_4$ < *anti*-$N_2H_4$.[65] In addition, mechanistic studies performed on metal surfaces, such as Ir,[95] Cu,[96] Ni[97–99] and Pt,[100] are consistent with the siligraphene trends.

In our study, a gauche adsorbed configuration was not obtained from structural optimization, which shows that C behaves differently to $SiC_3$ siligraphene and metals. Unlike in these studies, the different adsorption modes on defective graphene are driven by the lack of electron density. Hence, the *a*-SL structure only saturates one dangling carbon atom showing a weak adsorption energy ($E_{ADS}$ = −0.78 eV), whereas when two or more dangling bonds are saturated (*c*B–N and *c*B–H, respectively), the species are more strongly bonded to the surface.[101–104]

## Hydrazine decomposition

We considered two symmetric and one asymmetric dehydrogenation, and incomplete decomposition pathways based on previous reports.[19–21] However, only the most stable routes to the formation of $H_2$ and $NH_3$ was analysed in detail. The *c*B–H was the most stable adsorption configuration and the first step for complete hydrazine reforming (eqn (1)), whereas the *c*B–N was the first step towards an incomplete hydrazine decomposition (eqn (2)) (Fig. 4b and c). The difference in energy between the N–H and the N–N dissociative adsorptions indicated that the hydrogen production pathway was the preferred one ($\Delta E_{(NN-NH)}$ = 0.450 eV). Indeed, once the N–H bond was broken, a $C_3$–H was formed leading to hydrogen production. To proceed with dehydrogenation reaction mechanisms over continuous surfaces, *e.g.* graphene and metal slabs, we could consider a negligible activation energy for the migration of the dissociated H adatoms similar to the spill on metal catalysts.[105] However, the SV is a point defect, and the active site is isolated from adjacent dangling bonds. Thus, two different hydrogen production pathways were tested (Fig. 5). The first one, SWC-Decomposition (symmetric non-directional solvent complete decomposition, Fig. 5), simulated the absence of an alkaline aqueous medium and the H species needed to overcome a non-negligible diffusion energy barrier to free the active site. Hence, we investigated the H migration along three different paths (Fig. S3, ESI†) in a similar fashion to previous studies.[106–108]

For the most favourable migration pathway (Fig. S4, ESI†), we obtained a diffusion energy barrier of ($E_D$) 3.48 eV (Fig. S5, ESI†) in a polarizable continuum background, which did not provide a realistic directional solvation in aqueous solutions.[107]

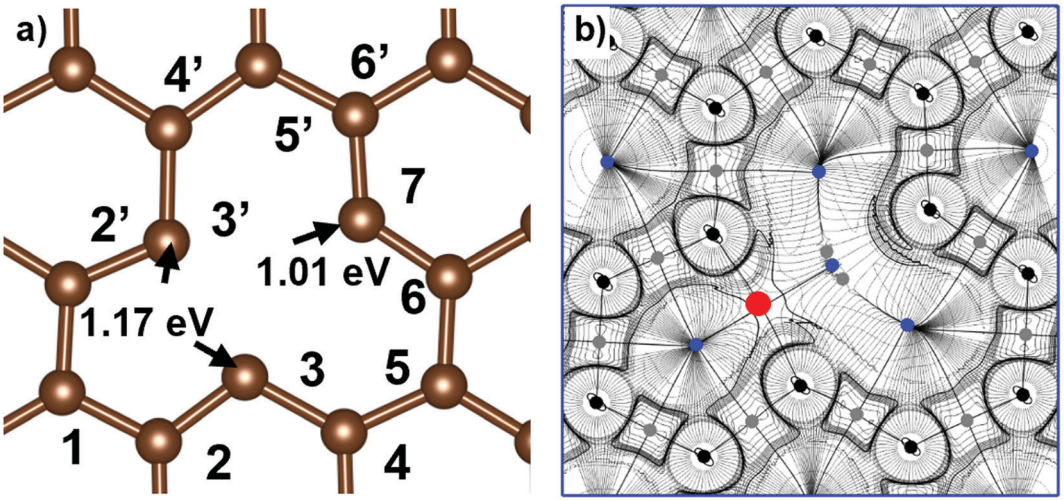


Fig. 3 Single vacancy representation. (a) Individual active sites and $NH_3$ relative adsorption energies. (b) Charge–density Laplacian analysis iso-surface plot; the red circle indicates the evaluation site for $\rho(\vec{r}_{BCP})$, black circles indicate nuclear charge density maxima, grey bond critical points and blue ring critical points.

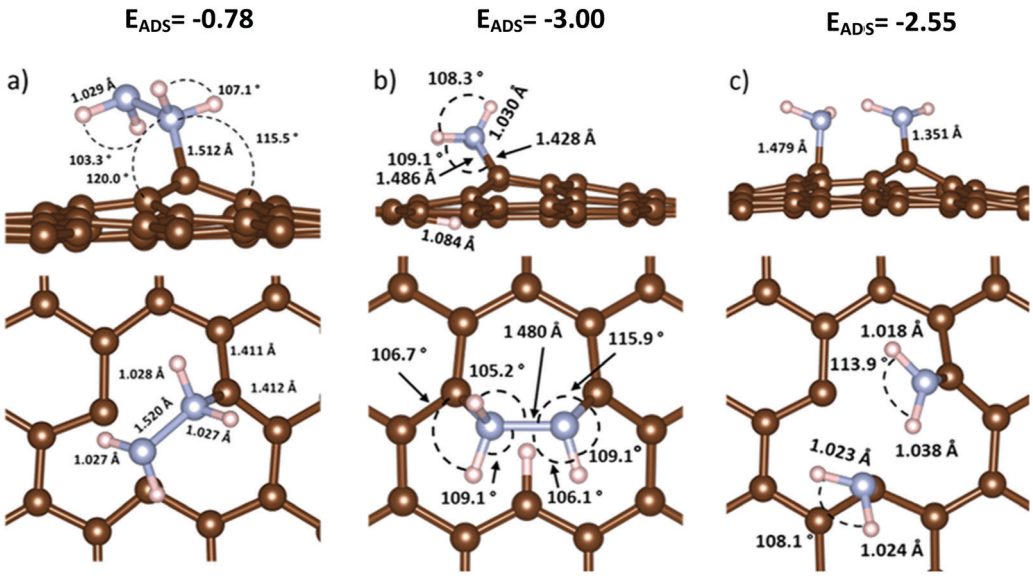


Fig. 4 Top and side views of the most favourable hydrazine configurations: (a) a-SL, (b) *c*B–H and (c) *c*B–N. Insets are the adsorption energies ($E_{ADS}$) and the main distances (Å) and angles (°) of interest. Carbon atom is labelled in brown, nitrogen in blue and hydrogen in white.

According to our simulations, two H atoms occupying nearest neighbor dangling carbon sites had an endothermic reaction energy ($E_R$ = 2.90 eV) to form $H_2$ (Fig. S6, ESI†). However, the experiments were performed in solution, which surrounded H* with an arranged (dipole) solvation shell promoting the H diffusion through the solution as well as the $H_2$ evolution through the Heyrovsky mechanism.[109] Thus, we considered the desorption from C3 (Fig. 3) negligible in comparison with the energy required to dissociate and form N–H and N–N bonds. The second mechanism tested for the release of $C_3$, SAC-decomposition (symmetric alkaline complete decomposition, Fig. 5), did not involve diffusion and recombination but the formation of water with the $OH^-$ groups. Indeed, sodium hydroxide could interact and promote the reactivation of the C site to proceed with the dehydrogenation steps.

### SWC $H_2$ production

Considering the diffusion and recombination of atomic hydrogen and thus the absence of NaOH, SWC-decomposition pathway was tested. The first dehydrogenation on the *c*B–H structure, common to both SAC and SWC pathways, presented an increment in the N centre $sp^3$ character and the N–N bond stretches by about 0.03 Å, while the N–H stretching was negligible. The $C_3$–N and $C_7$–N bond equilibrium lengths were not symmetric and differed by 0.058 Å. In addition, the initial SV site changed its structure to accommodate the adsorbed species (Fig. 6a and 7a). In the following step

 

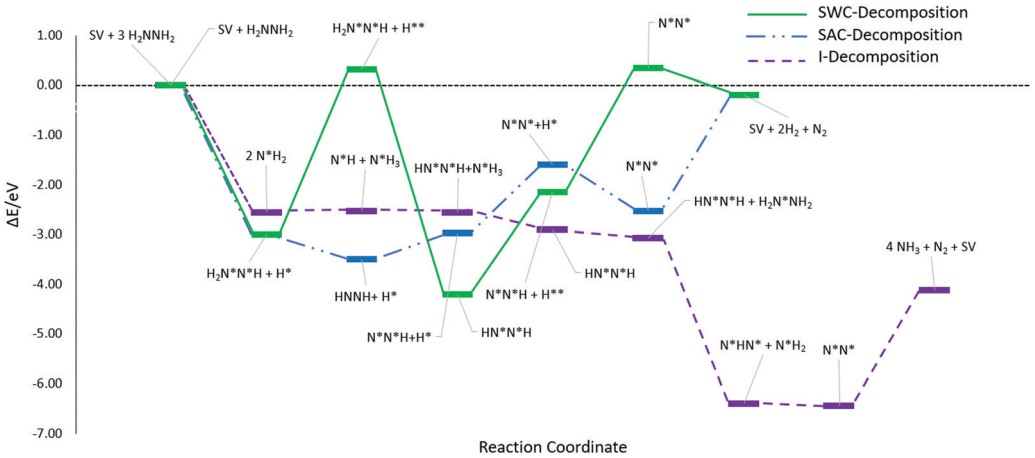


Fig. 5 Energy profiles for hydrazine decomposition pathways. Purple line indicates the incomplete decomposition pathway leading to $NH_3$(I-decomposition), blue and green lines indicate the two possibilities of symmetric dehydrogenation with NaOH and water (respectively SAC- and SWC-decomposition. In the SWC-decomposition pathway H** indicates diffused atomic hydrogen species, a single * is used to indicate which atom is adsorbed on the surface active sites.

along the SWC pathway, the adsorbed $H_2N^*N^*H$ intermediate may take three different dehydrogenation pathways: two symmetric and one asymmetric (Fig. 5). Among all symmetric decomposition pathways, SWC was the most favourable one, and for this reason, it will be the only one considered (Fig. 5, SWC-decomposition). Upon diffusion to the co-adsorbed H (Fig. 6b, $E_R$ = 3.319 eV), the intermediate HNNH (Fig. 6c) showed a N–N bond contraction of 0.037 Å and a reduction of the $C_3$–N and $C_7$–N bond lengths (0.094 Å and 0.005 Å, respectively). The superior stability of the adsorbed HN*N*H compared to the asymmetric counterpart, $H_2N^*N^*$ ($\Delta E_{Asymm-Symm}$ = 0.739 eV, Fig. S7, ESI†) could be related to the higher symmetry of the structure. The energy needed to overcome the $H_2$ in-vacancy recombination energy led to an endothermic step ($E_R$ = 1.066 eV). The subsequent step proceeded through the scission of another N–H bond (Fig. 6d). The dehydrogenated N centre assumed a $sp^2$ hybridization, *i.e.*, planar configuration. The structure obtained was exceptionally exothermic due to an overall dangling carbon saturation ($E_R$ of −3.625 eV). Nonetheless, the contribution of $E_D$ (+3.48 eV) slightly increased the reaction energy. In the final structure (Fig. 6e, $E_R$ = + 2.50 eV), the N–N bond showed an additional contraction indicating increasing sp hybridization, typical of molecular $N_2$, which spontaneously evolved from the surface freeing the active site ($E_R$ = −0.19 eV).

### SAC $H_2$ production

Here, in contrast to the SWC-decomposition pathway, the presence of NaOH is considered disregarding the H recombination–diffusion steps. In this case, OH– can interact with the adsorbed atomic hydrogen, freeing the active site and leading to the next dehydrogenation step. The presence of NaOH as alkaline medium (SAC) led to a more favourable dehydrogenation pathway (Fig. 5). Fig. 7 shows the SAC-decomposition mechanism where, in each step, the dangling bonds were completely saturated, increasing its stability. The dissociative adsorption step (Fig. 7a) was followed by a further hydrogen extraction (Fig. 7b, $E_R$ = −0.491 eV) due to the interaction with $OH^-$ ions, which presented an exothermic behaviour. Differently from the SWC, the formation of a $C_3$–H bond influenced both structures and energies ($\Delta E_{SWC-SAC}$ = 3.810 eV, Fig. 6b and 7b). The N–H and C–N bonds were more contracted, in particular, the C–N bonds respectively by 0.018 and 0.045 Å, while the N–H bonds by 0.004 and 0.013 Å. In the subsequent step (Fig. 7c, $E_R$ = 0.525 eV), further dehydrogenation was performed with the *in situ* evolution of a molecular hydrogen species. The C–N bond related to the bare N centre contracted by 0.085 Å, while either N–N or N–H bonds did not show any variation. Moreover, it is possible to observe that the bare N centre tilted towards the $C_3$–H. Overall, the step is slightly endothermic, due to the breakage of the N–H bond. Subsequently (Fig. 7d), the bare N centre bonded to $C_3$ and a scission of the N–H bond occurred and the atomic H bonded to a non-active C atom ($E_R$ = +1.377 eV). Indeed, from Fig. 7d it is possible to observe that the structure was deformed in order to bond the H atoms. The structure of the last dehydrogenation step (Fig. 7e) was completely equivalent to the one described in the SWC mechanism (Fig. 6e).

Nonetheless, from the energetic point view, the difference was mainly related to $H_2$ evolution. Indeed, in the SWC mechanism it was necessary to overcome the energetic barrier deriving from the in-vacancy recombination of two diffused H atoms ($E_R$ = 2.900 eV, Fig. S6, ESI†). Here, the hydrogen evolution did not require any recombination, leading to an exothermic step ($E_R$ = −0.937 eV). In the last step, $N_2$ evolution was endothermic and required overcoming an energetic barrier of 2.328 eV.

### $NH_3$ production

Hydrazine can be also decomposed into $NH_3$ and $N_2$ through the incomplete decomposition pathway (I-Decomposition), where three $N_2H_4$ molecules are involved. The first step of $NH_3$ production (Fig. 8a) involved the breakage of the N–N bond upon adsorption, forming the cB-N structure ($E_{ADS}$ = −2.55 eV). The two adsorbed $NH_2$ lay on the dangling carbons

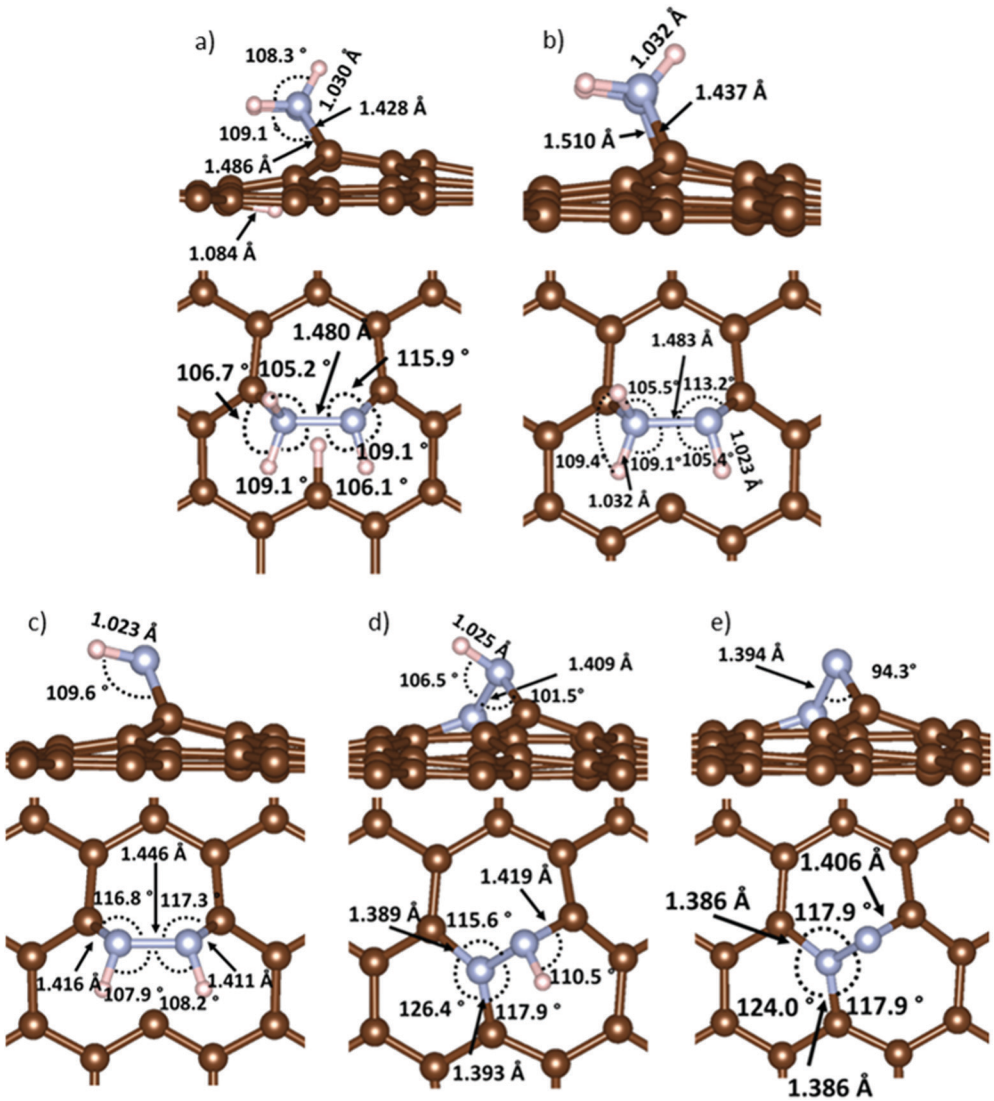


Fig. 6 Top and side views of the most favourable hydrazine configurations for $H_2$ production in water: (a) dissociative adsorption step N*$H_2$N*H + H*, (b) hydrogen diffusion step N*$H_2$N*H + H**, (c) second dehydrogenation step and $H_2$ evolution, N*HN* H, (d) third dehydrogenation step with diffusion, N*N* H + H** and (e) last dehydrogenation step, $H_2$ and $N_2$ evolution, N*N*. Inset, distances (Å) and angles (°) of interest. Carbon atoms are labelled in brown, nitrogen in blue and hydrogen in white.

with a $sp^3$-like configuration. The following elementary step consisted in a hydrogen transfer, involving the two N*$H_2$, followed by the $NH_3$ evolution. As can be seen from the structure in Fig. 8b, the remaining N*H tilted toward the vacancy center. A contraction of the free dangling carbons ($C_3$–$C_{3'}$) distance is then observed, leading to a slightly endothermic process ($E_R$ = +0.018 eV). To close the catalytic cycle, a subsequent hydrazine adsorption bridging between the available active sites was considered (Fig. 8c). The initial N*H took two hydrogen atoms from the second $N_2H_4$ in a concerted mechanism upon its adsorption, leading to the formation of HN*N*H + N*$H_3$. This step showed an overall exothermic energy ($E_R$ = −0.019 eV), along with the following $NH_3$ exothermic evolution process, leading HN*N*H on the SV (Fig. 8d, $E_R$ = −0.35 eV). In the subsequent elementary step, a third hydrazine could exothermically co-adsorb on the under-coordinated carbon sites $C_7$ ($E_R$ = −0.163 eV, Fig. 8e). In this position, the third hydrazine molecule interacted with an H of the adsorbed HN*N*H yielding a $NH_3$ molecule (Fig. 8e). The structure obtained is energetically favorable ($E_R$ = −3.33 eV, Fig. 8f) and the H-free N bridged between two carbon sites with a $sp^2$ hybridization. Instead, the $C_7$ atom was saturated connecting two N atoms, showing a conventional $sp^3$ geometry. The interaction between N*$H_2$ and the H located on the bridged HN*N* led to the evolution of the last $NH_3$ (Fig. 8f, $E_R$ = −0.05 eV). The resulting $N_2$ was anchored on the carbon lattice ($E_R$ = +2.32 eV) analogously to the SAC hydrogen production pathway.

Rationalizing the results obtained by combining experimental and DFT study the activity and the selectivity of the most performing material (PR24-PS) can be explained. In particular, the SV defect showed an exothermic adsorption energy in our

 

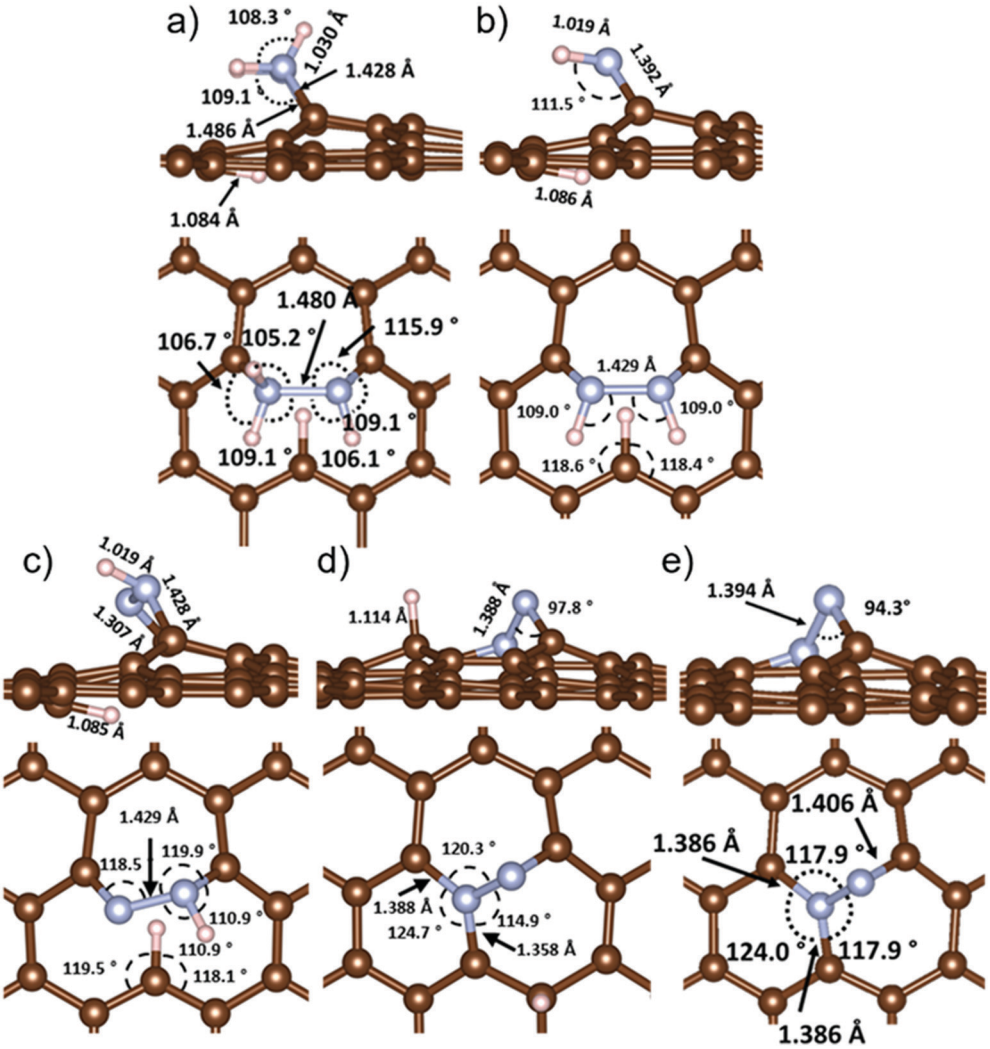


Fig. 7 Top and side views of the most favourable hydrazine configurations for $H_2$ production in the presence of aqueous NaOH: (a) Dissociative adsorption step N*H2N*H + H*, (b) dehydrogenation step: N*HN*H + H*, (c) second dehydrogenation step and $H_2$ evolution, N*N* H + H*, (d) third dehydrogenation step, N*N* + H* and (e) last dehydrogenation step, H2 and N2 evolution, N*N*. Inset, distances (Å) and angles (°) of interest. Carbon atoms are labelled in brown, nitrogen in blue and hydrogen in white.

substrate, indicating that it is the only defect which participates in the reaction. CNF-PS is the catalyst with a higher defectiveness degree, leading to the observed enhanced activity in the experimental results. Moreover, the investigation on the two complete dehydrogenation pathways (SWC- and SAC-decomposition) can explain the difference in the reaction rate changing the pH. Indeed, in the absence of NaOH the adsorbed atomic hydrogen needs to overcome the energetic barrier due to its diffusion and recombination, whereas in alkaline environment the $OH^-$ ions can interact with H*, freeing the active site and leading to next dehydrogenation step. Confirming that, a selectivity for $H_2$ of 89% at 94% conversion was found testing CNF-PS in the presence of NaOH. Considering the initial dissociative adsorption, the first step of the dehydrogenation pathway is more favorable (dissociation of the N–H bond, −3.00 eV) than the scission of the N–N bond (−2.55 eV) which leads to $NH_3$ as the product. This first reaction step is crucial to define the reaction mechanisms and the computational results fully agree with the ones obtained in the experiments.

## Conclusions

In this study, different metal-free carbonaceous materials, *i.e.* CNF PS, CNF HHT and graphite were tested in the hydrazine hydrate decomposition reaction for the first time. In addition, a systematic density functional theory (DFT) study on $N_2H_4$ adsorption and decomposition mechanisms was then employed to understand the role of the defects paving the pathway to the development of new and efficient carbocatalysts to be used in this reaction. A conversion of 94%, 71% and 65% was observed after 6 h of reaction for CNF PS, CNF HHT and graphite, respectively. To the best of our knowledge, this is the first work reported in the literature, which shows the ability of

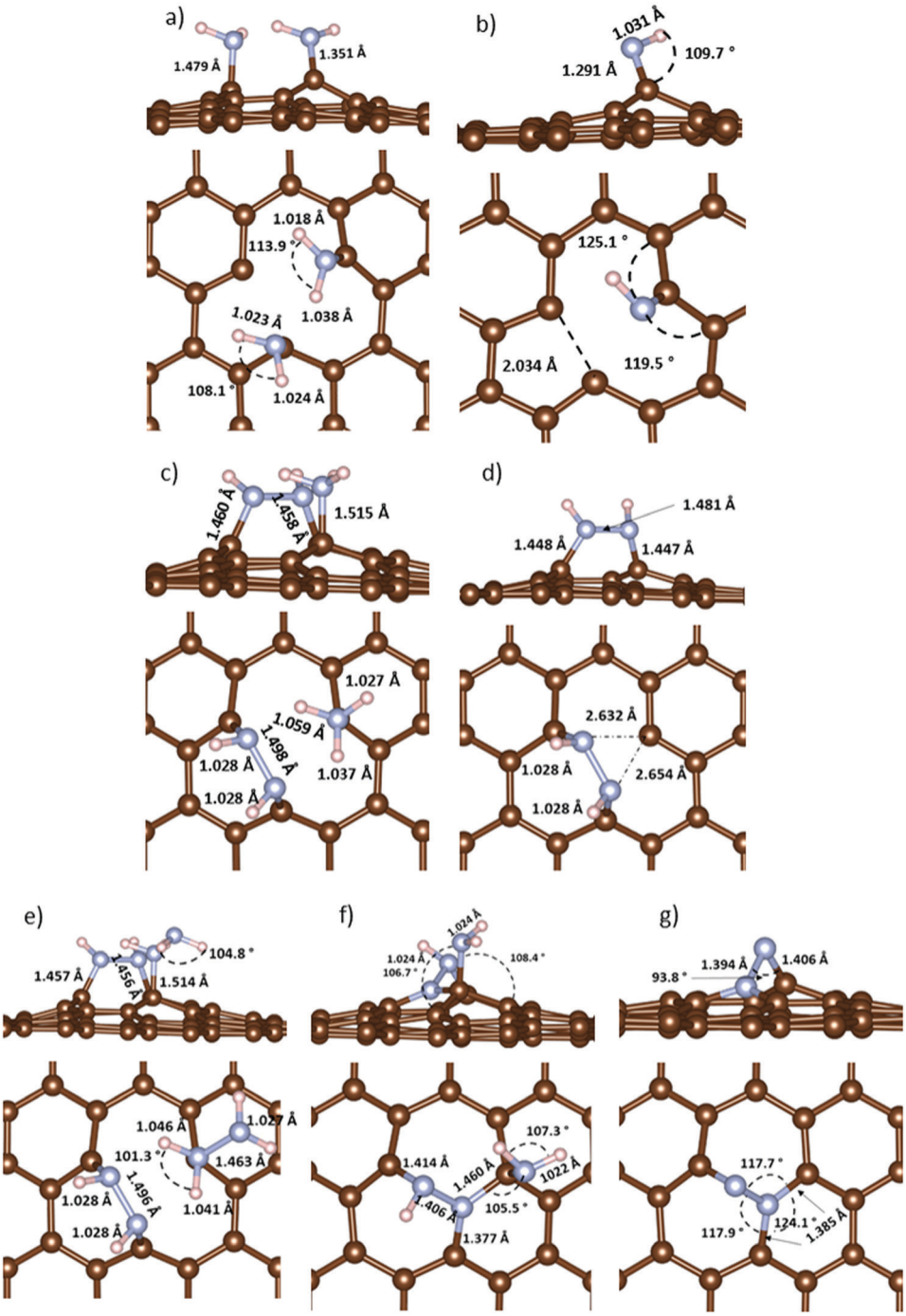


Fig. 8 Top and side views of the most favourable hydrazine configurations for $NH_3$ production: (a) N–N bond breakage step, 2 N*$H_2$, (b) First $NH_3$ evolution step, N*H, (c) second hydrazine adsorption step, N*HN*H + N*$H_3$, (d) second $NH_3$ evolution step, N*HN*H, (e) third hydrazine linkage step, N*HN*H + N*$H_2NH_2$, (f) third $NH_3$ evolution step, N*HN* + N*$H_2$ and (g) fourth $NH_3$ and $N_2$ evolution step, N*N*. Inset, distances (Å) and angles (°) of interest. Carbon atoms are labelled in brown, nitrogen in blue and hydrogen in white.

metal-free carbonaceous materials to decompose hydrazine hydrate. Moreover, a selectivity for $H_2$ of 89% at 94% conversion was found for CNF-PS. The materials were also analyzed using ICP and Raman spectroscopy. A correlation between the numbers of defects present in the catalysts and the initial activity of the hydrazine decomposition reaction was found. In particular, the initial activity increases with an increase in the number of defects, *i.e.* CNF-PS > CNF-HHT > graphite. Correlating the $I_D/I_G$ ratio obtained by Raman spectroscopy and the initial activity, a linear correlation was found. In addition, CNF PS was also tested in the absence of alkaline medium to understand the effect of NaOH. The catalyst showed a conversion (15% conversion at 4 h) lower than in the presence of NaOH (70% conversion at 4 h).

 

In order to understand the effect of the defects on the decomposition of hydrazine, different surfaces were modelled using DFT calculation, *i.e.* pristine graphene, single and double vacancies, and different Stone–Wales defects. According to our previous studies, only SV showed an exothermic adsorption energy for our substrate, indicating that it is the only defect, which participates in the reaction. Two symmetrical and one asymmetrical dehydrogenation pathways were found, but only the most favorable one (symmetric hydrazine dehydrogenation) was considered in our discussion. On the most stable hydrogen production pathway, the effect of the alkaline medium was elucidated through calculations concerning the diffusion and recombination of atomic hydrogen. Indeed, the presence of NaOH helps extraction of H species without additional energetic barriers, as opposed to the calculations performed in a polarizable continuum medium. In addition, an incomplete decomposition pathway forming $N_2$ and $NH_3$ was studied and compared with the dehydrogenation one. Considering the initial dissociative adsorption, the first step of the dehydrogenation pathway is more favorable (dissociation of the N–H bond, −3.00 eV) than the scission of the N–N bond (−2.55 eV) which leads to $NH_3$ as the product. This first reaction step is crucial to define the reaction mechanisms and the computational results fully agree with the ones obtained in the experiments. Moreover, comparing two different hydrogen production pathways (with and without diffusion and recombination), we confirmed that the presence of sodium hydroxide in the experimental reaction environment can modify the energy gap between the two pathways, leading to a selectivity to $H_2$ near 90%. Overall, this work provides a complete insight of hydrazine decomposition over intrinsic elementary defects of metal-free carbonaceous catalysts. Finally, these results can be used as a raw model for the synthesis of carbocatalysts with enhanced features for the liquid phase hydrazine decomposition reaction, focusing on widening the $\Delta E_{NN-NH}$ energy gap.

## Conflicts of interest

There are no conflicts to declare.

## Acknowledgements

We acknowledge computing time on the facilities of Supercomputing Wales and the Advanced Research Computing Cardiff (ARCCA) at Cardiff University.

## Notes and references

1 T. N. Veziroğlu and S. Şahin, *Energy Convers. Manage.*, 2008, **49**, 1820–1831.
2 P. Nikolaidis and A. Poullikkas, *Renewable Sustainable Energy Rev.*, 2017, **67**, 597–611.
3 M. Z. Chen, W. L. Zouyang, J. W. Liu, X. D. Yao, H. Wang and Z. W. Liu, *J. Power Sources*, 2017, **359**, 400–407.
4 I. Shown, A. Ganguly, L. C. Chen and K. H. Chen, *Energy Sci. Eng.*, 2015, **3**, 1–25.
5 K. Sordakis, C. Tang, L. K. Vogt, H. Junge, P. J. Dyson, M. Beller and G. Laurenczy, *Chem. Rev.*, 2018, **118**, 372–433.
6 H. J. Jeon and Y. M. Chung, *Appl. Catal., B*, 2017, **210**, 212–222.
7 M. Yadav and Q. Xu, *Energy Environ. Sci.*, 2012, **5**, 9698–9725.
8 S. K. Singh and Q. Xu, *J. Am. Chem. Soc.*, 2009, **131**, 18032–18033.
9 S. K. Singh, Z. Lu and Q. Xu, *Eur. J. Inorg. Chem.*, 2011, 2232–2237.
10 S. K. Singh, X.-B. Zhang and Q. Xu, *J. Am. Chem. Soc.*, 2009, **131**, 9894–9895.
11 S. K. Singh, A. K. Singh, K. Aranishi and Q. Xu, *J. Am. Chem. Soc.*, 2011, **133**, 19638–19641.
12 R. Lan, J. T. S. Irvine and S. Tao, *Int. J. Hydrogen Energy*, 2012, **37**, 1482–1494.
13 L. Giorgi, A. Pozio, C. Bracchini, R. Giorgi and S. Turtù, *J. Appl. Electrochem.*, 2001, **31**, 325–334.
14 M. Pravica, L. Bai and Y. Liu, *Chem. Phys. Lett.*, 2013, **555**, 115–118.
15 A. S. Shteinberg, in *High-Temperature Decomposition and Thermal Explosion of Liquid Propellant Components: Hydrogen Peroxide and Hydrazine*, ed. A. S. Shteinberg, Springer Berlin Heidelberg, Berlin, Heidelberg, 2008, pp. 173–198.
16 J. K. Norskov and C. H. Christensen, *Science*, 2006, **312**, 1322 LP–1323 LP.
17 S. E. Wood and J. T. Bryant, *Prod. R&D*, 1973, **12**, 117–122.
18 T. G. Soares Neto, A. J. G. Cobo and G. M. Cruz, *Appl. Catal., A*, 2003, **250**, 331–340.
19 J. P. Contour and G. Pannetier, *J. Catal.*, 1972, **24**, 434–445.
20 R. Maurel and J. C. Menezo, *J. Catal.*, 1978, **51**, 293–295.
21 P.-X. Zhang, Y.-G. Wang, Y.-Q. Huang, T. Zhang, G.-S. Wu and J. Li, *Catal. Today*, 2011, **165**, 80–88.
22 A. K. Singh, M. Yadav, K. Aranishi and Q. Xu, *Int. J. Hydrogen Energy*, 2012, **37**, 18915–18919.
23 L. Zhou, X. Luo, L. Xu, C. Wan and M. Ye, *Catalysts*, 2020, **10**, 930.
24 L. He, B. Liang, L. Li, X. Yang, Y. Huang, A. Wang, X. Wang and T. Zhang, *ACS Catal.*, 2015, **5**, 1623–1628.
25 M. Zheng, R. Cheng, X. Chen, N. Li, L. Li, X. Wang and T. Zhang, *Int. J. Hydrogen Energy*, 2005, **30**, 1081–1089.
26 S. K. Singh and Q. Xu, *Catal. Sci. Technol.*, 2013, **3**, 1889–1900.
27 Y. Cheng, X. Wu and H. Xu, *Sustainable Energy Fuels*, 2019, **3**, 343–365.
28 Z. Zhang, S. Zhang, Q. Yao, X. Chen and Z.-H. Lu, *Inorg. Chem.*, 2017, **56**, 11938–11945.
29 S. J. Cho, J. Lee, Y. S. Lee and D. P. Kim, *Catal. Lett.*, 2006, **109**, 181–186.
30 H.-L. Jiang, S. K. Singh, J.-M. Yan, X.-B. Zhang and Q. Xu, *ChemSusChem*, 2010, **3**, 541–549.
31 P. Z. Li and Q. Xu, *J. Chinese Chem. Soc.*, 2012, **59**, 1181–1189.
32 Y.-P. Qiu, H. Yin, H. Dai, L.-Y. Gan, H.-B. Dai and P. Wang, *Chem. – Eur. J.*, 2018, **24**, 4902–4908.

33 Y.-Y. Jiang, H.-B. Dai, Y.-J. Zhong, D.-M. Chen and P. Wang, *Chem. – Eur. J.*, 2015, **21**, 15439–15445.
34 P. Zhao, N. Cao, J. Su, W. Luo and G. Cheng, *ACS Sustainable Chem. Eng.*, 2015, **3**, 1086–1093.
35 Y. B. Jang, T. H. Kim, M. H. Sun, J. Lee and S. J. Cho, *Catal. Today*, 2009, **146**, 196–201.
36 X. Du, P. Cai, W. Luo and G. Cheng, *Int. J. Hydrogen Energy*, 2017, **42**, 6137–6143.
37 N. Cao, L. Yang, H. Dai, T. Liu, J. Su, X. Wu, W. Luo and G. Cheng, *Inorg. Chem.*, 2014, **53**, 10122–10128.
38 R. Jiang, X. Qu, F. Zeng, Q. Li, X. Zheng, Z. Xu and J. Peng, *Int. J. Hydrogen Energy*, 2019, **44**, 6383–6391.
39 L. He, B. Liang, Y. Huang and T. Zhang, *Natl. Sci. Rev.*, 2018, **5**, 356–364.
40 L. He, Y. Huang, X. Y. Liu, L. Li, A. Wang, X. Wang, C.-Y. Mou and T. Zhang, *Appl. Catal., B*, 2014, **147**, 779–788.
41 Y. Qiu, H. Yin, H. Dai, L. Gan, H. Dai and P. Wang, *Chem. – Eur. J.*, 2018, **24**, 4902–4908.
42 J. Chen, Q. Yao, J. Zhu, X. Chen and Z.-H. Lu, *Int. J. Hydrogen Energy*, 2016, **41**, 3946–3954.
43 Y. Jiang, H. Dai, Y. Zhong, D. Chen and P. Wang, *Chem. – Eur. J.*, 2015, **21**, 15439–15445.
44 H. Wang, L. Wu, Y. Wang, X. Li and Y. Wang, *Catal. Commun.*, 2017, **100**, 33–37.
45 S. N. Oliaee, C. Zhang, S. Y. Hwang, H. M. Cheung and Z. Peng, *J. Phys. Chem. C*, 2016, **120**, 9764–9772.
46 J. Wang, X.-B. Zhang, Z.-L. Wang, L.-M. Wang and Y. Zhang, *Energy Environ. Sci.*, 2012, **5**, 6885–6888.
47 U. Sikander, S. Sufian and M. A. Salam, *Int. J. Hydrogen Energy*, 2017, **42**, 19851–19868.
48 Z. Liu, J. Li, S. Xue, S. Zhou, K. Qu, Y. Li and W. Cai, *J. Energy Chem.*, 2020, **47**, 317–323.
49 C. Li and J. B. Baek, *ACS Omega*, 2020, **5**, 31–40.
50 X. Zhou, Y. Huang, W. Xing, C. Liu, J. Liao and T. Lu, *Chem. Commun.*, 2008, 3540–3542.
51 M. Mavrikakis, J. A. Herron, J. Scaranto, P. Ferrin and S. Li, *ACS Catal.*, 2014, **4**, 4434–4445.
52 N. Gupta, O. Khavryuchenko, A. Villa and D. Su, *ChemSusChem*, 2017, **10**, 3030–3034.
53 P. Veerakumar, P. Thanasekaran, T. Subburaj and K.-C. Lin, *C*, 2018, **4**, 54.
54 M. M. Titirici and M. Antonietti, *Chem. Soc. Rev.*, 2010, **39**, 103–116.
55 G. Mestl, N. I. Maksimova, N. Keller, V. V. Roddatis and R. Schlögl, *Angew. Chem., Int. Ed.*, 2001, **40**, 2066–2068.
56 J. Zhang, X. Liu, R. Blume, A. Zhang, R. Schlögl and D. S. Su, *Science*, 2008, **322**, 73–78.
57 J. Zhang, D. S. Su, R. Blume, R. Schlögl, R. Wang, X. Yang and A. Gajović, *Angew. Chem., Int. Ed.*, 2010, **49**, 8640–8644.
58 J. H. Yang, G. Sun, Y. Gao, H. Zhao, P. Tang, J. Tan, A. H. Lu and D. Ma, *Energy Environ. Sci.*, 2013, **6**, 793–798.
59 D. R. Dreyer, H. P. Jia and C. W. Bielawski, *Angew. Chem., Int. Ed.*, 2010, **49**, 6813–6816.
60 M. A. Patel, F. Luo, M. R. Khoshi, E. Rabie, Q. Zhang, C. R. Flach, R. Mendelsohn, E. Garfunkel, M. Szostak and H. He, *ACS Nano*, 2016, **10**, 2305–2315.
61 A. Primo, F. Neatu, M. Florea, V. Parvulescu and H. Garcia, *Nat. Commun.*, 2014, **5**, 1–9.
62 Y. Gao, D. Ma, C. Wang, J. Guan and X. Bao, *Chem. Commun.*, 2011, **47**, 2432–2434.
63 I. Barlocco, S. Capelli, X. Lu, S. Tumiati, N. Dimitratos, A. Roldan and A. Villa, *Nanoscale*, 2020, **12**, 22768–22777.
64 X. Lu and A. Roldan, *J. Phys. Chem. C*, 2021, **125**, 15950–15958.
65 F. Zheng, H. Dong, Y. Ji and Y. Li, *Appl. Surf. Sci.*, 2019, **469**, 316–324.
66 C. Gojon and B. Dureault, *J. Nucl. Sci. Technol.*, 1996, **33**, 731–735.
67 W. D. Basson and J. F. Van Staden, *Analyst*, 1978, **103**, 998–1001.
68 G. Kresse and J. Furthmüller, *Phys. Rev. B: Condens. Matter Mater. Phys.*, 1996, **54**, 11169–11186.
69 G. Kresse, *J. Non Cryst. Solids*, 1995, **192–193**, 222–229.
70 B. Hammer, L. B. Hansen and J. K. Nørskov, *Phys. Rev. B*, 1999, **59**, 7413–7421.
71 N. D. Mermin, *Phys. Rev.*, 1965, **137**, 1–3.
72 Y. Zhang and W. Yang, *Phys. Rev. Lett.*, 1998, **80**, 890.
73 R. Sure, J. Antony and S. Grimme, *J. Phys. Chem. B*, 2014, **118**, 3431–3440.
74 S. Ehrlich, J. Moellmann, W. Reckien, T. Bredow and S. Grimme, *ChemPhysChem*, 2011, **12**, 3414–3420.
75 H. Fang, A. Roldan, C. Tian, Y. Zheng, X. Duan, K. Chen, L. Ye, S. Leoni and Y. Yuan, *J. Catal.*, 2019, **369**, 283–295.
76 X. Lu, S. Francis, D. Motta, N. Dimitratos and A. Roldan, *Phys. Chem. Chem. Phys.*, 2020, **22**, 3883–3896.
77 E. Nowicka, S. Althahban, T. D. Leah, G. Shaw, D. Morgan, C. J. Kiely, A. Roldan and G. J. Hutchings, *Sci. Technol. Adv. Mater.*, 2019, **20**, 367–378.
78 M. G. Quesne, A. Roldan, N. H. De Leeuw and C. R. A. Catlow, *Phys. Chem. Chem. Phys.*, 2019, **21**, 10750–10760.
79 R. Sundararaman and K. Schwarz, *J. Chem. Phys.*, 2017, **146**, 084111.
80 K. Mathew, R. Sundararaman, K. Letchworth-Weaver, T. A. Arias and R. G. Hennig, *J. Chem. Phys.*, 2014, **140**, 084106.
81 J. D. Pack and H. J. Monkhorst, *Phys. Rev. B*, 1977, **16**, 1748–1749.
82 Y. W. Tan, H. L. Stormer, P. Kim, K. S. Novoselov, M. L. Cohen, S. G. Louie, X. Wang, L. Zhang, S. Lee, H. Dai, Y. Kobayashi, K. Fukui, M. Fujita, G. Dresselhaus, M. S. Dresselhaus, M. A. Pimenta, B. R. A. Neves, A. Jorio, Y. Zhang, M. Mailman, P. M. Ajayan, S. K. Nayak, C. H. Park, Y. W. Son, S. P. Lu, S. Piscanec, A. C. Ferrari, G. Dobrik, P. Lambin, A. Oberlin, T. Solid, K. Suenaga, S. Iijima, P. Hermet, V. Meunier, L. Henrard, D. Gunlycke, C. T. White, S. Chen, B. I. Yakobson and S. Gradecak, *Science*, 2009, **323**, 1705–1708.
83 G. Henkelman, A. Arnaldsson and H. Jónsson, *Comput. Mater. Sci.*, 2006, **36**, 354–360.
84 M. Yu and D. R. Trinkle, *J. Chem. Phys.*, 2011, **134**, 1–8.
85 P. L. A. Popelier, *Coord. Chem. Rev.*, 2000, **197**, 169–189.
86 D. Vega and D. Almeida, *J. Comput. Methods Sci. Eng.*, 2014, **14**, 131–136.

 

87 V. A. Borodin, T. T. Vehviläinen, M. G. Ganchenkova and R. M. Nieminen, *Phys. Rev. B: Condens. Matter Mater. Phys.*, 2011, **84**, 1–15.
88 F. Tuinstra and J. L. Koenig, *J. Chem. Phys.*, 1970, **53**, 1126–1130.
89 C. R. Wick and T. Clark, *J. Mol. Model.*, 2018, **24**, 1–9.
90 L. Ma, J. M. Zhang, K. W. Xu and V. Ji, *Appl. Surf. Sci.*, 2015, **343**, 121–127.
91 X. Y. Liu, J. M. Zhang, K. W. Xu and V. Ji, *Appl. Surf. Sci.*, 2014, **313**, 405–410.
92 S. Yang, Z. Lan, H. Xu, G. Lei, W. Xie and Q. Gu, *J. Nanotechnol.*, 2018, **2018**, 8457670.
93 D. C. de Oliveira, W. O. Silva, M. Chatenet and F. H. B. Lima, *Appl. Catal., B*, 2017, **201**, 22–28.
94 B. Luo, T. Wu, L. Zhang, F. Diao, Y. Zhang, L. Ci, J. Ulstrup, J. Zhang and P. Si, *Electrochim. Acta*, 2019, **317**, 449–458.
95 X. Lu, S. Francis, D. Motta, N. Dimitratos and A. Roldan, *Phys. Chem. Chem. Phys.*, 2020, **22**, 3883–3896.
96 S. S. Tafreshi, A. Roldan and N. H. de Leeuw, *Phys. Chem. Chem. Phys.*, 2015, **17**, 21533–21546.
97 M. K. Agusta and H. Kasai, *Surf. Sci.*, 2012, **606**, 766–771.
98 H. Yin, Y.-P. Qiu, H. Dai, L.-Y. Gan, H.-B. Dai and P. Wang, *J. Phys. Chem. C*, 2018, **122**, 5443–5451.
99 M. K. Agusta, M. David, H. Nakanishi and H. Kasai, *Surf. Sci.*, 2010, **604**, 245–251.
100 M. K. Agusta, W. A. Diño, M. David, H. Nakanishi and H. Kasai, *Surf. Sci.*, 2011, **605**, 1347–1353.
101 L. Liu, M. Qing, Y. Wang and S. Chen, *J. Mater. Sci. Technol.*, 2015, **31**, 599–606.
102 D. W. Boukhvalov and M. I. Katsnelson, *Nano Lett.*, 2008, **8**, 4373–4379.
103 A. Eftekhari and H. Garcia, *Mater. Today Chem.*, 2017, **4**, 1–16.
104 G. Cantele, Y.-S. Lee, D. Ninno and N. Marzari, *Nano Lett.*, 2009, **9**, 3425–3429.
105 D. Zhao, D. Lü, Y. Zang and X. Zhao, *Prog. Chem.*, 1997, **9**, 759–788.
106 C. P. Herrero and R. Ramírez, *Phys. Rev. B: Condens. Matter Mater. Phys.*, 2009, **79**, 1–8.
107 Y. Lei, S. A. Shevlin, W. Zhu and Z. X. Guo, *Phys. Rev. B: Condens. Matter Mater. Phys.*, 2008, **77**, 1–8.
108 L. Chen, A. C. Cooper, G. P. Pez and H. Cheng, *J. Phys. Chem. C*, 2007, **111**, 18995–19000.
109 E. Skúlason, V. Tripkovic, M. E. Björketun, S. Gudmundsdóttir, G. Karlberg, J. Rossmeisl, T. Bligaard, H. Jónsson and J. K. Nørskov, *J. Phys. Chem. C*, 2010, **114**, 18182–18197.